Magnetic Resonance Imaging 60 (2019) 122–129

Contents lists available at ScienceDirect

Magnetic Resonance Imaging

journal homepage: www.elsevier.com/locate/mri

Original contribution

Ultrafast multi-slice chemical exchange saturation transfer imaging scheme based on segmented spatiotemporal encoding

Jizhou Cai, Jian Wu, Chenlu Guo, Shuhui Cai*, Congbo Cai*

Department of Electronic Science, Fujian Provincial Key Laboratory of Plasma and Magnetic Resonance, Xiamen University, Xiamen, China

ARTICLE INFO

Keywords:
Chemical exchange saturation transfer
MRI
Multi-slice
Spatiotemporal encoding

ABSTRACT

Chemical exchange saturation transfer (CEST) imaging is an important magnetic resonance molecular imaging technology. However, long acquisition time limits its clinical application, especially when multi-slice CEST imaging is needed. Though single-shot EPI can be used to accelerate CEST imaging, images are often distorted under inhomogeneous magnetic fields. In this work, we propose a new method called CEST-SeSPEN for ultrafast multi-slice CEST imaging based on segmented spatiotemporally encoded (SeSPEN) MRI. Experiments were performed on creatine phantom and hen egg. The results show that CEST-SeSPEN can provide good CEST contrast images. Its acquisition time is much shorter than other multi-slice CEST methods currently available. It may be used in challenging situation where high temporal resolution and robustness to field inhomogeneity are vital.

1. Introduction

Chemical exchange saturation transfer (CEST) [1–5] is a technique emerged in the MRI field. CEST MRI can quantitatively characterize the chemical exchange between labile protons in proteins or metabolites and bulk water protons. Over the past decades, due to its unique quantitative contrast mechanism, CEST MRI has been successfully used in detecting pathological and chemical changes in a variety of diseases, such as human cranial nervous system diseases [6,7], cerebral ischemia in animals [8–10], and tumors [11–14].

The frequency offsets of exchangeable protons usually range from 0 to 5 ppm relative to the water resonance [15]. For example, the hydroxyl protons are mainly at 1 ppm, the amine protons are at approximately 2 ppm, and the amide protons are at about 3.5 ppm [16–20]. To obtain a CEST contrast image, we need to perform multiple scans by setting a plurality of saturation pulses with different frequencies, and then draw a Z-spectrum and calculate the CEST effect based on the acquired images. Z-spectrum, which is used to characterize the CEST effect quantitatively, is a curve describing the relationship between normalized water signal intensity and offset frequency ($\Delta\omega$) from water resonance (the $\Delta\omega$ of water signal is set as 0 ppm). To measure the difference between the signals on the two sides of Z-spectrum after the saturation pulse is applied, the magnetization transfer ratio (MTR) is commonly used, which is defined as: $MTR_{asym} = [S_{sat}(-\Delta\omega) - S_{sat}(-\Delta\omega)] / S_0$, where $S_{sat}(-\Delta\omega)$ and $S_{sat}(\Delta\omega)$ denote the water signal intensity when a saturation pulse is applied at $-\Delta\omega$ and $\Delta\omega$, respectively, and S_0 is the water signal intensity without any saturation pulse applied. The duration of the saturation pulse and repetition time (TR) typically last for a few seconds, which lead to long acquisition time and limit the clinical application of CEST MRI accordingly, hence a rapid imaging technique is crucial to the CEST MRI, especially when multi-slice imaging is needed.

Most of the CEST MRI sequences include a saturation module and an image readout module. The image readout module typically employs fast imaging sequence such as fast spin echo (FSE) or echo planar imaging (EPI) [15,21–24]. Generally, the scan time for FSE to collect a Z-spectrum is on the order of minutes. EPI can greatly shorten the scan time for a Z-spectrum, but it also faces many restrictions, especially from the field inhomogeneity, which will affect the CEST contrast results and thus hinder its application. Moreover, in practical application, multi-slice CEST MRI is often needed, which will greatly prolong the scan time. Spatiotemporally encoded (SPEN) MRI has stronger ability in resisting inhomogeneous field and chemical shift effects than EPI while retaining the advantage of time resolution of EPI [25,26]. A SPEN MRI method has been proposed to accelerate CEST imaging and obtained satisfactory results [27]. However, this method is only suitable for single-slice imaging.

In this study, we propose a new method (dubbed CEST-SeSPEN MRI) for ultrafast multi-slice CEST imaging based on segmented spatiotemporally encoded (SeSPEN) MRI [28]. This method enables multi-

* Corresponding authors at: Department of Electronic Science, Xiamen University, Xiamen, China.
E-mail addresses: shcai@xmu.edu.cn (S. Cai), cbcai@xmu.edu.cn (C. Cai).

https://doi.org/10.1016/j.mri.2019.04.004
Received 6 December 2018; Received in revised form 29 March 2019; Accepted 2 April 2019

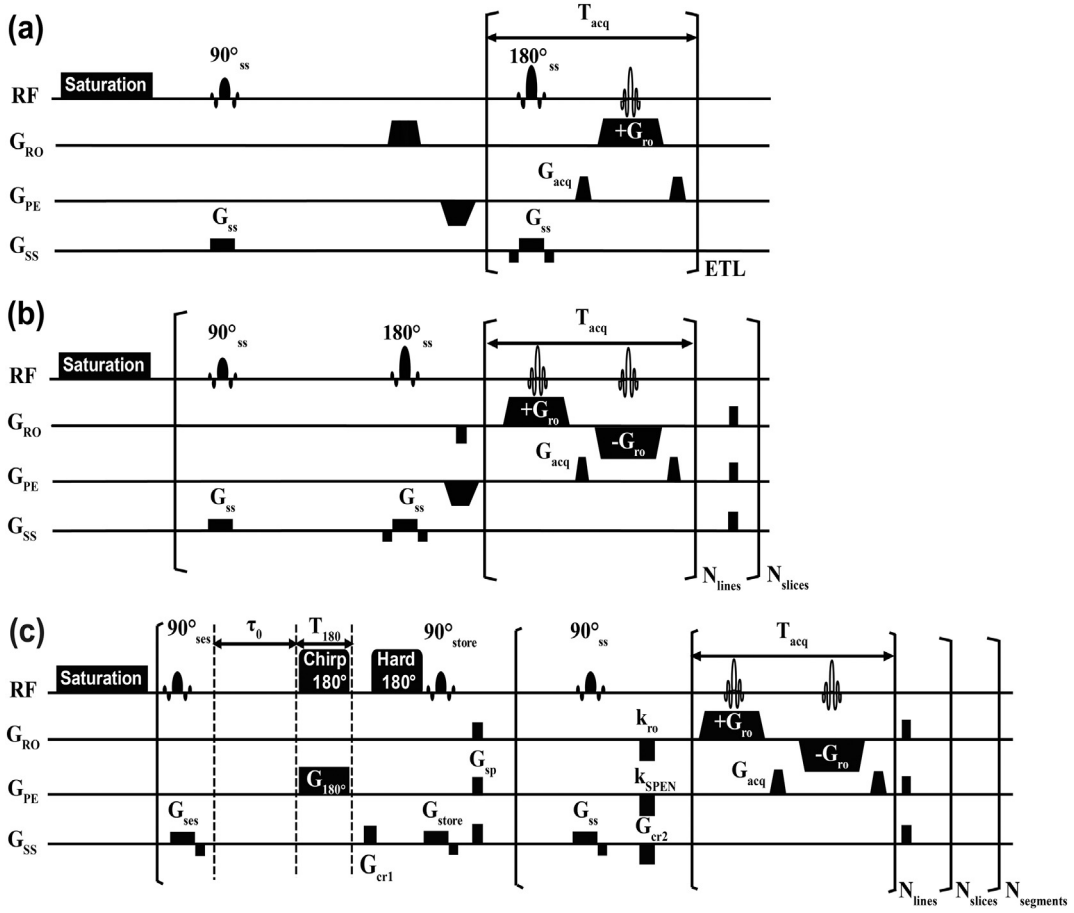

Fig. 1. CEST MRI sequences. (a) CEST-FSE sequence, ETL = 8; (b) single-shot CEST-EPI sequence; (c) single-shot CEST-SeSPEN sequence. Abbreviations: ETL, echo train length; G_{RO}, readout direction; G_{PE}, phase/SPEN direction; G_{SS}, slice selective direction; acq, acquisition; ses, segment selective; ss, slice selective; ro, readout; cr, crusher; sp, spoiler. $N_{segments}$, N_{slices} and N_{lines} are numbers of selected segments, selected slices and spatiotemporally decoded elements.

slice CEST imaging in a single shot, and greatly shortens the acquisition time.

2. Material and methods

2.1. Principle of segmented spatiotemporally encoded imaging

As shown in Fig. 1c, the CEST-SeSPEN sequence consists of a continuous wave (CW) saturation pulse and a SeSPEN acquisition module. The CW saturation pulse is used to produce steady CEST effect, and SeSPEN enables ultrafast multi-slice acquisition by segmenting slice selection dimension [28].

Primarily, the entire imaged object is segmented along the slice selection dimension (z direction) through the 90° segment-selective radio-frequency (RF) pulse ($90°_{ses}$). The thickness of each segment, which is composed of several slices, is determined according to the thickness and the number of slices that need to be scanned in it. Only the spins in the targeted segment are excited by the first RF pulse, and then spatiotemporally encoded by the 180° chirp pulse. In the following, the effects of chemical shift, background inhomogeneous field, transverse relaxation and diffusion are neglected. Assuming that the 180° chirp pulse sweeps the targeted field of view (FOV) L_y linearly and symmetrically, we can obtain the quadratic phase of the excited spins along the SPEN dimension (y direction) after the 180° chirp pulse [28]:

$$\varphi_{180}(y) = -\frac{\gamma G_{180} T_{180}}{L_y} y^2 - \frac{\gamma G_{180} T_{180} L_y}{4} \tag{1}$$

where γ represents the gyromagnetic ratio, G_{180} and T_{180} denote the amplitude and duration of the encoding gradient, respectively. In the meantime, the spins in the untargeted segment will be flipped to -z direction by the 180° chirp pulse. Subsequently, a 180° hard pulse is employed to restore the spins that are not targeted by the $90°_{ses}$ pulse back to the thermodynamically stable state for subsequent segment selection and acquisition. The 180° hard pulse also flips all the other spins. The quadratic phase of the spins in the targeted segment after the 180° hard pulse evolves into the following form [28]:

$$\varphi_1(y) = \frac{\gamma G_{180} T_{180}}{L_y} y^2 + \frac{\gamma G_{180} T_{180} L_y}{4} - \gamma G_{cr1} T_{cr1} y \tag{2}$$

where G_{cr1} and T_{cr1} represent the magnitude and duration of the first crusher gradient in Fig. 1c, respectively. Subsequently, a 90° selective pulse ($90°_{store}$), which is the same as the $90°_{ses}$ pulse, is applied to store the spatiotemporally encoded information. Next we can successively acquire the signals of every slice in the encoded region along the z direction with the help of slice-selective pulse ($90°_{ss}$). The $90°_{ss}$ divides the targeted segment into several slices without inter-slice gap.

According to the principle of spatiotemporal encoding, for full decoding, the acquisition gradient G_{acq} and the acquisition time T_{acq} must satisfy the following equation [29]:

$$2 \cdot G_{180} T_{180} = \int_0^{T_{acq}} G_{acq}(t)\, dt \tag{3}$$

The signal of the *k*th slice in the targeted segment can be expressed as following:

$$S^k(t) \propto \int_{-L_y/2}^{L_y/2} M^k(y) \cdot \frac{-e^{i\varphi_1(y)} - e^{-i\varphi_1(y)}}{2} \cdot e^{i(\gamma G_{cr2} T_{cr2} y + k_{SPEN} y + \gamma G_{acq} y t)} \cdot e^{-\tau_k/T_1} dy \tag{4}$$

where $M^k(y)$ indicates the transverse proton magnetization per unit volume of bulk water at position y in the kth slice, k_{SPEN} is the initial purging gradient with an area of $|k_{SPEN}| = \gamma G_{180} T_{180}$, which is used to shift the position of the minimum of the spin phase parabola in k-space, τ_k denotes the time interval between the 90°$_{store}$ pulse and the kth slice-selective pulse, T_1 indicates the longitudinal relaxation time, and G_{cr2} and T_{cr2} represent the amplitude and duration of the second crusher gradient, respectively. According to the stationary phase principle [26], the acquired signal of the kth slice can be simplified to

$$|S^k(t)| \propto M^k(y_{spp}) \cdot \Delta y \cdot e^{-\tau_k/T_1} \tag{5}$$

where Δy denotes the size of the imaged pixel, and y_{spp} denotes the stationary phase point. The stationary phase point y_{spp} is related to the acquisition time t via the formula $y_{spp} = L_y t/T_{acq} - L_y/2$ [28]. Since the intrinsic spatial resolution of the original image based on spatio-temporal encoding is relatively low, the de-convolution algorithm is applied for super-resolved (SR) reconstruction [30]. Owing to the use of full-refocusing, CEST-SeSPEN can enormously reduce the influence of field inhomogeneity and chemical shift [31].

2.2. Quantification of CEST

MTR_{asym} method is commonly used to measure the difference between the signals on the two sides of Z-spectrum. However, in some biological tissues, such as egg, conventional magnetization transfer (MT) effect and nuclear Overhauser enhancement (NOE) effect also exist other than CEST. Meanwhile, the signal frequency shift caused by magnetic field inhomogeneity and random noises are often reflected in the Z-spectrum. Therefore, we do not use MTR_{asym} method to calculate the CEST in this study. Several methods have been proposed to fit the Z-spectrum to reduce the impact of field inhomogeneity and random noises [32–36]. Among these methods, the commonly used one is to perform Lorentzian fitting centered at the water peak [15]:

$$L(\Delta\omega) = \frac{A\alpha^2}{\alpha^2 + 4(\Delta\omega - \delta)^2} + b \tag{6}$$

where $L(\Delta\omega)$ is the value of Lorentzian curve at $\Delta\omega$, A is the maximum amplitude of the Lorentzian curve, α is the linewidth of water peak, δ is the frequency shift of water peak due to magnetic field inhomogeneity, and b is a constant to approximately counteract the global baseline migration of the MT effect in the Z-spectrum [37]. In this work, partial Lorentzian fitting was applied (see Fig. 2), the regions $|\Delta\omega| \leq 1$ ppm and 5 ppm $\leq |\Delta\omega| \leq 6$ ppm were used to avoid the influence of strong CEST/amide proton transfer (APT) CEST effect. After fitting, we can separate CEST/APT CEST effect from the MT [38], which enables us to calculate the CEST/APT CEST effect subsequently [27]. The frequency offsets of exchangeable protons usually range from 0 to 5 ppm relative to the water resonance, so the CEST effect can be expressed as following formula:

$$CEST = \sum_{\Delta\omega=0}^{5} [L(\Delta\omega) - S_{sat}(\Delta\omega)] \tag{7}$$

After quantitative CEST values are calculated, the CEST contrast images can be reconstructed accordingly.

2.3. Sample preparation

Amine protons of creatine have a frequency offset of 2 ppm downfield from water, exhibiting a significant CEST effect. Therefore, a phantom containing four tubes of creatine solution with different concentration was used to prove the feasibility of CEST-SeSPEN. The concentrations of creatine solution were 20 mM, 40 mM, 60 mM and 80 mM, respectively (pH = 7.2). Fresh hen eggs can roughly mimic biological tissues, and egg white is a gelatinous, semitransparent liquid mixture with about 11% proteins [39], so they were used to demonstrate the APT effect.

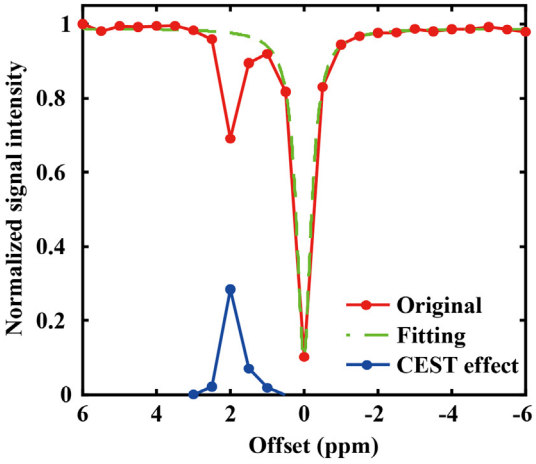

Fig. 2. Schematic diagram of Lorentzian fitting of the Z-spectrum of a water solution of creatine (80 mM). The red solid line represents the original Z-spectrum, the green dash line demonstrates the partial Lorentzian fitting curve, and the blue solid line (obtained from original minus fitting) indicates the CEST effect. (For interpretation of the references to colour in this figure legend, the reader is referred to the web version of this article.)

2.4. Data acquisition

To evaluate the feasibility of CEST-SeSPEN, the experimental results of the CEST-EPI sequence (Fig. 1b) were used for comparison, and the results of the CEST-FSE sequence (Fig. 1a) were used as references.

Experiments were performed on a 7 T MRI system (Agilent Technologies, Santa Clara, California) at 298 K, with a horizontal Magnex magnet, equipped with 10 cm bore imaging gradients (40 G/cm). Both phantom experiments and hen egg experiments were conducted after careful field shimming, and the full width at half maximum (FWHM) of water peak was 49.37 Hz for creatine phantom and 87.23 Hz for egg.

Experimental parameters were set as follows: acquisition matrix = 64 × 64, slice number = 20, slice thickness of creatine phantom = 1.0 mm, slice thickness of egg = 1.0 mm. Following previous reports [40–42], we set power of RF saturation pulse = 1.8 μT/1.2 μT and saturation time = 2 s/4 s for creatine/egg respectively, and repetition time = 6 s. There was no gap between two adjacent slices. In all Z-spectrum experiments, the frequency of the saturation pulse was swept from −6 ppm to 6 ppm with an increment of 0.5 ppm for a total of 25 frequencies. In CEST-SeSPEN experiments, the bandwidth and duration of the 180° chirp pulse were 4 kHz and 15 ms, respectively, and two segments were acquired (ten slices in each segment). For CEST-FSE experiments, the total scan time of creatine/egg for a single slice was 27 min/33 min. For CEST-EPI and CEST-SeSPEN experiments, the total scan time of creatine/egg for 20 slices was 200 s/250 s. All data post-processing was carried out on MATLAB (The MathWorks, Natick, Massachusetts). After zero-filling in k-space and two-dimensional Fourier reconstruction, the matrix size of all reconstructed images of FSE and EPI was 256 × 256. The SeSPEN images had the same matrix size after de-convolution SR reconstruction. Theoretically, a large matrix size will help to improve the quality of reconstructed image. However, the reconstruction time will greatly increase correspondingly. Since the matrix size of 256 × 256 already gives pretty good reconstruction result, we chose it for reconstruction. The Lorentzian fitting was applied to the image point by point to obtain an accurate CEST contrast image. The threshold of the Lorentzian fitting is set as the

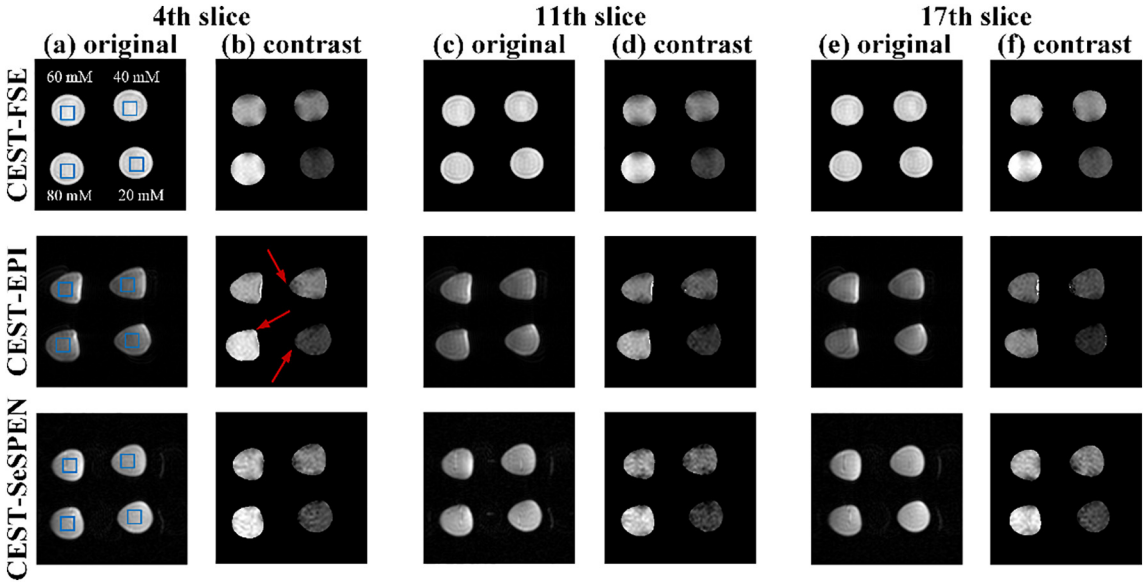

Fig. 3. Images of four-tube creatine solution phantom acquired with different CEST sequences. FOV = 45 × 45 mm^2. (a, c, e) Original images of the 4th, 11th, and 17th slices; (b, d, f) CEST contrast images of the 4th, 11th, and 17th slices at 2 ppm downfield from water peak. The images at the top, middle and bottom rows were obtained with CEST-FSE, CEST-EPI, and CEST-SeSPEN, respectively. The concentration of four creatine solutions are indicated in (a). The ROIs indicated with blue rectangles are used to calculate the CEST effects of creatine phantom. (For interpretation of the references to colour in this figure legend, the reader is referred to the web version of this article.)

quarter of the maximum normalized signal intensity to remove the background noises. All Z-spectrum analyses were calculated for a selected region of interest (ROI).

3. Results

3.1. Phantom validation

The imaging results of the creatine phantom are shown in Fig. 3. Because CEST-FSE sequence would take a long time to acquire 20 slices, only the 4th, 11th and 17th slices are acquired for comparison. It can be seen from Fig. 3 (red arrows) that the CEST contrast results from CEST-EPI display more severe geometric distortion, while the results from CEST-SeSPEN reveal preferable outlines, indicating that CEST-SeSPEN can alleviate image distortion. Compared with CEST-EPI, The CEST contrast of CEST-SeSPEN is better distributed, especially for the 17th slice. The CEST results of the 4th slice of creatine phantom obtained with different imaging sequences are shown in Fig. 4. The corresponding ROIs are indicated with blue rectangles in Fig. 3a. We can see that, compared with CEST-EPI, the CEST peaks at 2 ppm from CEST-SeSPEN are closer to those from CEST-FSE for all concentrations. However, the lineshapes from CEST-SeSPEN show lower similarity to CEST-FSE, especially at low concentration. Perhaps it is because SeSPEN is less robust to noise.

3.2. Hen egg study

The APT CEST imaging results of fresh hen egg are shown in Fig. 5. Similar to phantom experiments, only the results of 4th, 11th and 17th slices are given. It can be seen that the APT CEST contrast images obtained by CEST-EPI display severer distortion (red arrow), while those obtained with CEST-SeSPEN remain good shapes. For the 4th slice, the APT CEST contrast image from CEST-EPI shows signal loss, while CEST-SeSPEN can alleviate this situation (yellow arrow). The APT CEST curves of different slices of egg white are shown in Fig. 6 (the ROIs are shown in Fig. 5). We can see that the APT CEST curves show that the APT CEST effects obtained with the three sequences are close for the 4th slice. However, for the 11th and 17th slices, the APT CEST effect declines in the EPI result in comparison with the SeSPEN result. There are several possible reasons for this phenomenon: 1) the acquisition time of EPI is longer than SeSPEN. The latter slices of EPI will suffer from more influence of saturation recovery compared with SeSPEN. 2) EPI has lower robustness to inhomogeneous field, which results in a decline of APT CEST effect due to frequency shifting [27].

4. Discussion

CEST-SeSPEN can shorten the acquisition time of multi-slice CEST imaging while maintaining good robustness to magnetic field inhomogeneity compared with CEST-EPI. In our experiments, the bandwidth along the phase-encoded dimension is 2.28 kHz for CEST-EPI, 4.31 kHz for CEST-SeSPEN. Since CEST-SeSPEN has a larger bandwidth in the phase-encoded direction, our method is more robust to field inhomogeneity effect than CEST-EPI (Figs. 3 and 5). It can obtain more accurate CEST/APT CEST effect (Fig. 6). However, the increase of bandwidth will lead to the increase of noise, thus decreasing the signal-to-noise ratio (SNR). Considering the SNR problem on 7 T small animal imaging system, we did not choose larger bandwidth for SeSPEN.

To compare the SNRs of original CEST-EPI and CEST-SeSPEN results, the results of hen egg were used. The SNR is defined as [43]:

$$SNR(\mathbf{u}) = \frac{mean\{S_i(\mathbf{u})\}}{STD\{S_i(\mathbf{u})\}} \quad (i = 1, 2, ..., R) \tag{8}$$

where $S(\mathbf{u})$ is the signal intensity of pixel $\mathbf{u}$, R represents the number of repetition scans (R = 16 in this work), *mean* and *STD* stand for the average and standard deviation of signal intensity in the same pixel for R repetitions. The resulting SNR maps are given in Fig. 7a and b. They are normalized to the same scale. The corresponding mean SNR variation curves along the readout direction are shown in Fig. 7c. Each mean SNR is obtained by averaging the SNRs of all pixels in the pixel column along the phase-encoded direction. Comparing the SNR of different slice in a same segment (11th slice vs. 17th slice), we can see that the former slice has higher SNR than the latter slice for EPI, whereas the SNRs of both slices are close to each other for SeSPEN. Between different methods, the SNRs from SeSPEN are lower than those from EPI. In addition to the use of a larger bandwidth, the decrease of SNR in

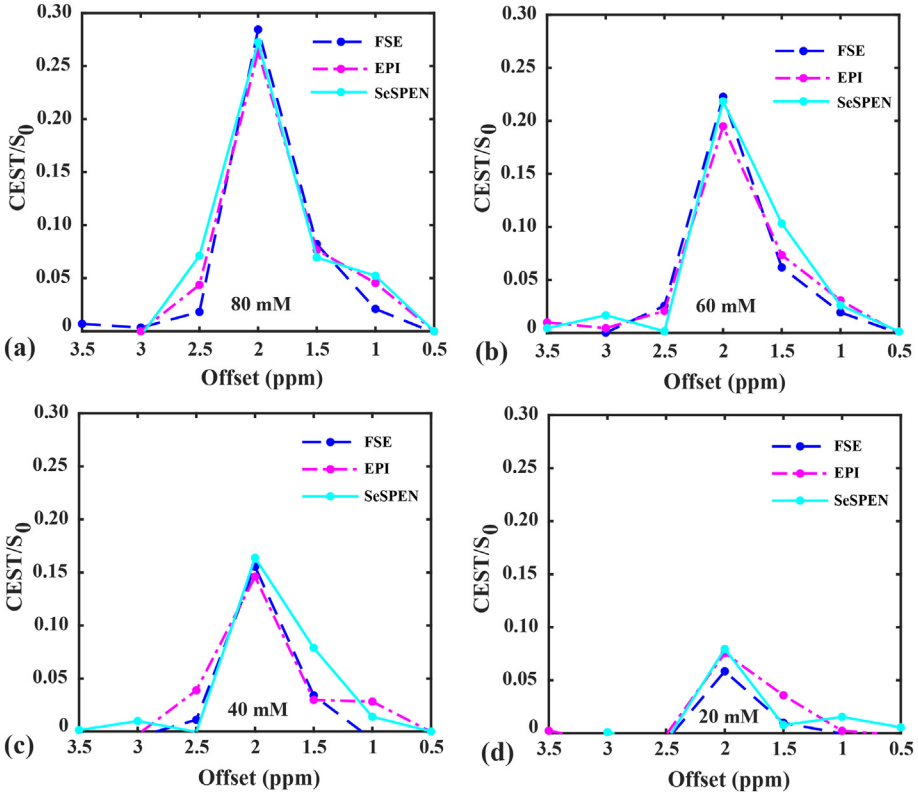

Fig. 4. CEST results of creatine phantom (the 4th slice) obtained with different imaging sequences. (a) Results for 80 mM creatine solution; (b) results for 60 mM creatine solution; (c) results for 40 mM creatine solution; (d) results for 20 mM creatine solution.

SeSPEN is also caused by a loss of half of the magnetization due to the use of 90° storage pulse aiming to flip the excited magnetization from transverse back to longitudinal direction. Moreover, the 180° hard pulse and 180° chirp pulse may not revert the unexcited spins back to the thermal equilibrium state completely, which will result in signal loss of the second segment. Usually, the volume of pixel imaged on 3 T human imaging system is 100 times larger than that on 7 T small animal imaging system, so the SNR problem may not be so serious at 3 T clinical field. On the other hand, the total variation regularization may be applied in de-convolution algorithm to smooth noise, thus enhancing the SNR [44].

According to Eq. (5), for the kth slice, the water signal intensity without any saturation pulse applied ($S_0{}^k(t)$) and the water signal intensity after a saturation pulse is applied ($S_{sat}{}^k(t)$) can be expressed as

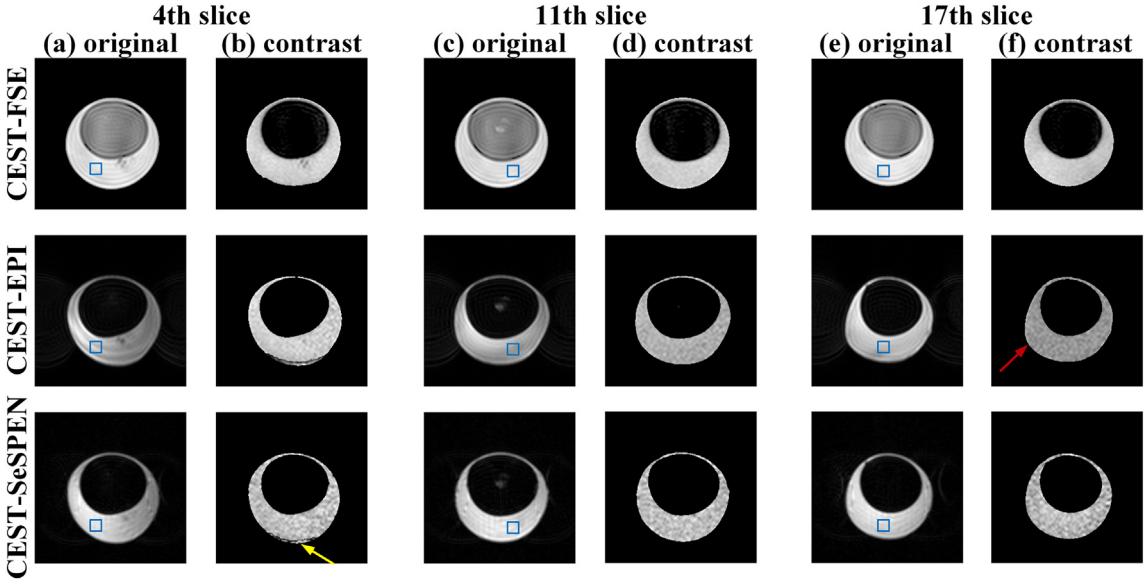

Fig. 5. Images of fresh hen egg acquired with different CEST sequences. FOV = 75 × 75 mm^2. (a, c, e) Original images of the 4th, 11th, and 17th slices; (b, d, f) APT CEST contrast images of the 4th, 11th, and 17th slices. The images at the top, middle and bottom rows were obtained with CEST-FSE, CEST-EPI, and CEST-SeSPEN, respectively. The ROIs indicated with blue rectangles are used to calculate the APT CEST effects of hen egg. (For interpretation of the references to colour in this figure legend, the reader is referred to the web version of this article.)

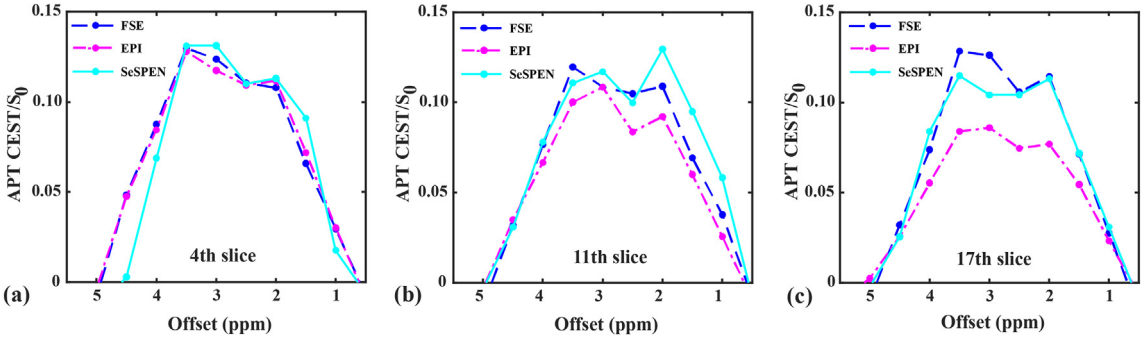

Fig. 6. APT CEST results of different slices of hen egg obtained with different imaging sequences. (a) Results for the 4th slice; (b) results the 11th slice; (c) results for the 17th slice.

$$|S_0^k(t)| \propto M_0^k(y_{spp})\cdot\Delta y\cdot e^{-\tau_k/T_1} \tag{9}$$

$$|S_{sat}^k(t)| \propto M_{sat}^k(y_{spp})\cdot\Delta y\cdot e^{-\tau_k/T_1} \tag{10}$$

where $M_0{}^k$ denotes the initial proton magnetization per unit volume of bulk water without any saturation pulse, $M_{sat}{}^k$ is the proton magnetization per unit volume of bulk water after the saturation pulse. It can be seen that the signal intensity will decrease with the increase of slice number due to T_1 relaxation. The Z-spectrum of the kth slice at any frequency point can be expressed as

$$S_{sat}^k(t)/S_0^k(t) = M_{sat}^k(y_{spp})/M_0^k(y_{spp}) \tag{11}$$

Although Eq. (11) does not include the $e^{-\tau_k/T_1}$ term, the Z-spectrum is still influenced by T_1 relaxation since $M_{sat}(y_{spp})$ is time-dependent [45]. However, the acquisition time of CEST-SeSPEN is only about 600 ms for 20 slices. The short acquisition time will reduce the effect from T_1 relaxation. All CEST contrast images of creatine solution phantom of the 20 slices are shown in Fig. 8. Clear contrast can be seen for the four tubes in any slice, and most slices show close contrast for any tube with same sample concentration despite the presence of T_1 relaxation. According to previous report [46], when the T_1 value is around 3 s (which is the case for our samples), good CEST results can be obtained if the acquisition time is shorter than 1 s. Therefore, the CEST/APT CEST effect of different slices obtained from CEST-SeSPEN is not obviously affected by T_1 relaxation.

5. Conclusions

CEST provides a unique MRI contrast mechanism and can be used to detect exchangeable protons. In this study, we propose an ultrafast multi-slice CEST imaging method based on spatiotemporal encoding technique, and demonstrate its feasibility and advantage through creatine phantom and hen egg experiments. The experimental results show that the new method can provide good CEST or APT CEST contrast images. It is more robust to magnetic field inhomogeneity than EPI. Its acquisition time is much faster than other multi-slice CEST methods currently available. With further optimization, it may find application in challenging situation where robustness to field inhomogeneity is concerned.

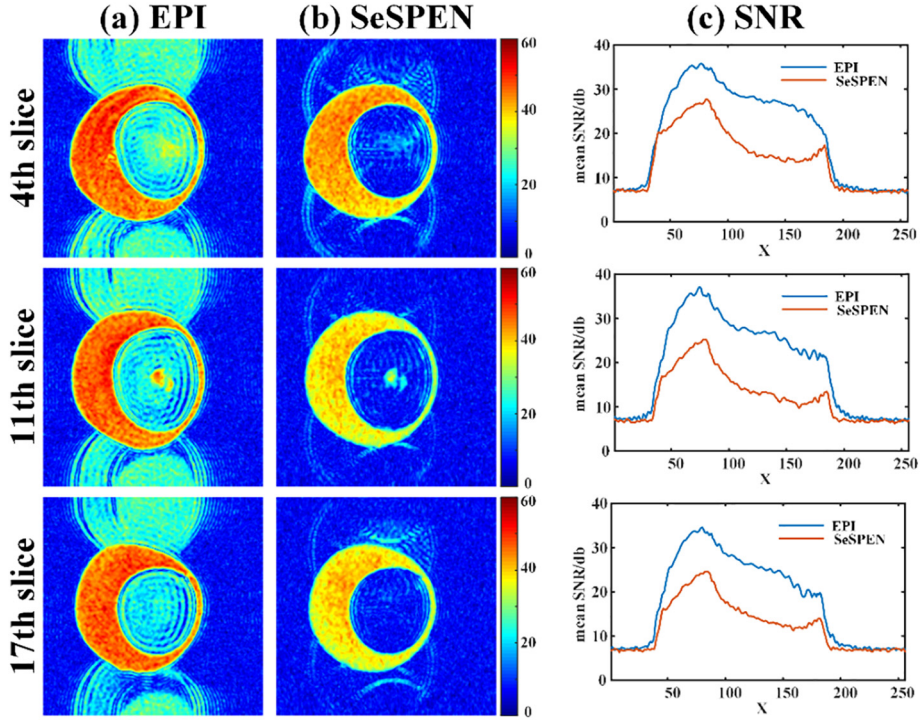

Fig. 7. Comparison of SNR maps from different imaging sequences. (a) SNR maps from EPI; (b) SNR maps from SeSPEN; (c) mean SNR curves along the readout direction (i.e. from left to right along the horizontal direction).

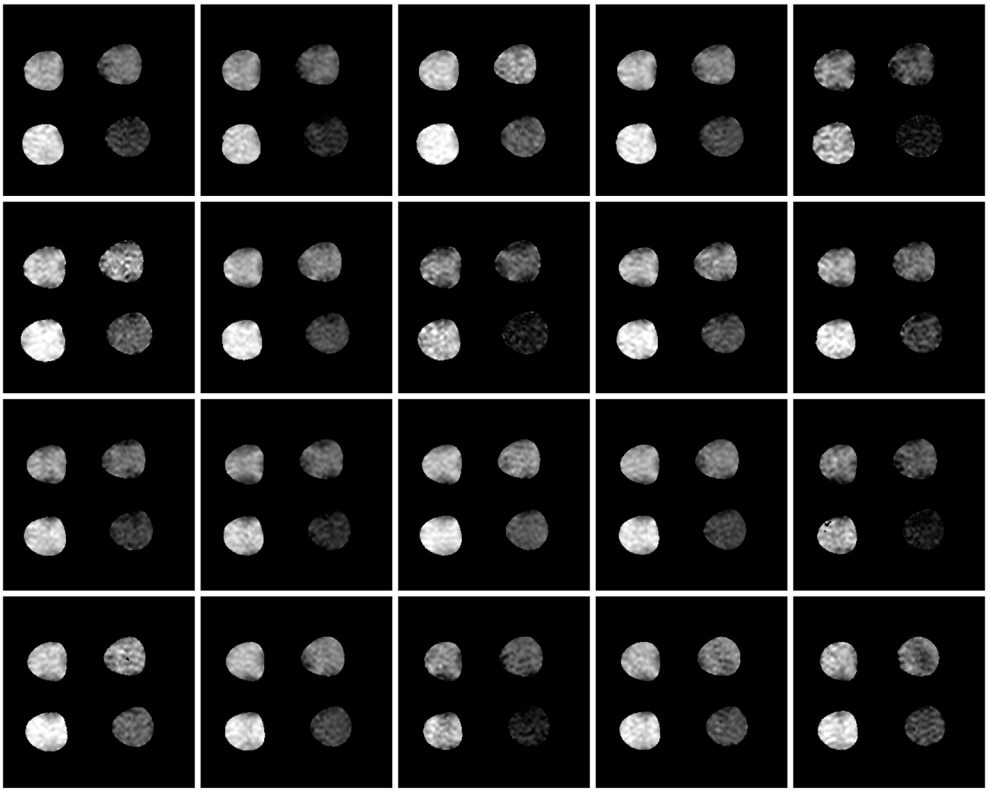

Fig. 8. CEST contrast images of creatine solution phantom of different slices obtained from CEST-SeSPEN. The slices from 1 to 20 are given from left to right and top to bottom.

Acknowledgments

This work was supported by the National Natural Science Foundation of China under Grants 11775184, 11474236 and 81671674.

References

[1] Aime S, Castelli DD, Crich SG, Gianolio E, Terreno E. Pushing the sensitivity envelope of lanthanide-based magnetic resonance imaging (MRI) contrast agents for molecular imaging applications. Acc Chem Res 2009;42:822–31.
[2] Ali MM, Liu G, Shah T, Flask CA, Pagel MD. Using two chemical exchange saturation transfer magnetic resonance imaging contrast agents for molecular imaging studies. Acc Chem Res 2009;40:915–24.
[3] Hancu I, Dixon WM, Vinogradov E, Sherry AD, Lenkinski RE. CEST and PARACEST MR contrast agents. Acta Radiol 2010;51:910–23.
[4] Zhou J, van Zijl PC. Chemical exchange saturation transfer imaging. Magn Reson Spectrosc 2016;48:109–36.
[5] Lu JH, Cai CB, Cai SH, Chen Z, Zhou J. Chemical exchange saturation transfer MRI using intermolecular double-quantum coherences with multiple refocusing pulses. Magn Reson Imaging 2014;32:759–65.
[6] Li C, Peng S, Wang R, Chen H, Su W, Zhao X, et al. Chemical exchange saturation transfer MR imaging of Parkinson's disease at 3 Tesla. Eur Radiol 2014;24:2631–9.
[7] Yuwen IZ, Wang E, Cheung JS, Lu D, Ji Y, Zhang X, et al. Direct saturation-corrected chemical exchange saturation transfer MRI of glioma: simplified decoupling of amide proton transfer and nuclear overhauser effect contrasts. Magn Reson Med 2017;78:2307–14.
[8] Zhou J, Erik T, Wen Z, Bachchu L, Zhou T, Rachel G, et al. Differentiation between glioma and radiation necrosis using molecular magnetic resonance imaging of endogenous proteins and peptides. Nat Med 2011;17:130–4.
[9] Sun PZ, Zhou J, Sun W, Huang J, van Zijl PC. Detection of the ischemic penumbra using pH-weighted MRI. J Cereb Blood Flow Metab 2007;27:1129–36.
[10] Jin T, Wang P, Zong X, Kim SG. Magnetic resonance imaging of the Amine-Proton EXchange (APEX) dependent contrast. Neuroimage 2012;59:1218–27.
[11] Cai K, Singh A, Poptani H, Li W, Yang S, Lu Y, et al. CEST signal at 2 ppm (CEST@ 2 ppm) from Z-spectral fitting correlates with creatine distribution in brain tumor. NMR Biomed 2015;28:1–8.
[12] Zhou J, Lal B, Wilson DA, Laterra J, van Zijl PC. Amide proton transfer (APT) contrast for imaging of brain tumors. Magn Reson Med 2003;50:1120–6.
[13] Jia G, Abaza R, Williams JAD, Zynger DL, Zhou J, Shah ZK, et al. Amide proton transfer MR imaging of prostate cancer: a preliminary study. J Magn Reson Imaging 2015;33:647–54.
[14] Chan KWY, Mcmahon MT, Kato Y, Liu G, Bulte JW, Bhujwalla ZM, et al. Natural D-glucose as a biodegradable MRI contrast agent for detecting cancer. Magn Reson Med 2012;68:1764–73.
[15] Jones CK, Polders D, Hua J, Zhu H, Hoogduin HJ, Zhou J, et al. In vivo three-dimensional whole-brain pulsed steady-state chemical exchange saturation transfer at 7 T. Magn Reson Med 2012;67:1579–89.
[16] Zhou J, Payen JF, Wilson DA, Traystman RJ, van Zijl PC. Using the amide proton signals of intracellular proteins and peptides to detect pH effects in MRI. Nat Med 2003;9:1085–90.
[17] van Zijl PC, Jones CK, Ren J, Malloy CR, Sherry AD. MRI detection of glycogen in vivo by using chemical exchange saturation transfer imaging (glycoCEST). Proc Natl Acad Sci U S A 2007;104:4359–64.
[18] Lindeman LR, Randtke EA, High RA, Jones KM, Howison CM, Pagel MD. A comparison of exogenous and endogenous CEST MRI methods for evaluating in vivo pH. Magn Reson Med 2018;79:2766–72.
[19] Zaiss M, Windschuh J, Goerke S, Paech D, Meissner JE, Burth S, et al. Downfield-NOE-suppressed amide-CEST-MRI at 7 Tesla provides a unique contrast in human glioblastoma. Magn Reson Med 2017;77:196–208.
[20] Mohammad H, Nanga RPR, Anup S, Kejia C, Feliks K, Hari H, et al. Exchange rates of creatine kinase metabolites: feasibility of imaging creatine by chemical exchange saturation transfer MRI. NMR Biomed 2012;25:1305–9.
[21] Shah T, Lu L, Dell KM, Pagel MD, Griswold MA, Flask CA. CEST-FISP: a novel technique for rapid chemical exchange saturation transfer MRI at 7 T. Magn Reson Med 2011;65:432–7.
[22] Sun PZ, Wang E, Cheung JS, Zhang X, Benner T, Sorensen AG. Simulation and optimization of pulsed radio frequency irradiation scheme for chemical exchange saturation transfer (CEST) MRI-demonstration of pH-weighted pulsed-amide proton CEST MRI in an animal model of acute cerebral ischemia. Magn Reson Med 2011;66:1042–8.
[23] Harris RJ, Yao J, Chakhoyan A, Raymond C, Leu K, Liau LM, et al. Simultaneous pH-sensitive and oxygen-sensitive MRI of human gliomas at 3 T using multi-echo amine proton chemical exchange saturation transfer spin-and-gradient echo echo-planar imaging (CEST-SAGE-EPI). Magn Reson Med 2018;80:1962–78.
[24] Li J, Zhang M, Chen L, Cai CB, Sun HJ, Cai SH. Reduced field-of-view imaging for single-shot MRI with an amplitude-modulated chirp pulse excitation and Fourier transform reconstruction. Magn Reson Imaging 2015;33:503–15.
[25] Ben-Eliezer N, Irani M, Frydman L. Super-resolved spatially encoded single-scan 2D MRI. Magn Reson Med 2010;63:1594–600.
[26] Tal A, Frydman L. Single-scan multidimensional magnetic resonance. Magn Reson Spectrosc 2010;57:241–92.
[27] Huang JP, Zhang M, Lu JH, Cai CB, Chen L, Cai SH. A fast chemical exchange saturation transfer imaging scheme based on single-shot spatiotemporal encoding. Magn Reson Med 2016;77:1786–96.

[28] Zhang T, Chen L, Huang JP, Li J, Cai SH, Cai CB, et al. Ultrafast multi-slice spatiotemporally encoded MRI with slice-selective dimension segmented. J Magn Reson 2016;269:138–45.
[29] Schmidt R, Frydman L. New spatiotemporal approaches for fully-refocused, multi-slice ultrafast 2D MRI. Magn Reson Med 2014;71:711–22.
[30] Cai CB, Dong JY, Cai SH, Li J, Chen Y, Bao LJ, et al. An efficient de-convolution reconstruction method for spatiotemporal-encoding single-scan 2D MRI. J Magn Reson 2013;228:136–47.
[31] Ben-Eliezer N, Shrot Y, Frydman L. High-definition, single-scan 2D MRI in inhomogeneous fields using spatial encoding methods. Magn Reson Imaging 2010;28:77–86.
[32] Yadav NN, Jones CK, Hua J, Xu J, van Zijl PC. Imaging of endogenous exchangeable proton signals in the human brain using frequency labeled exchange transfer imaging. Magn Reson Med 2013;69:966–73.
[33] Xu X, Yadav NN, Zeng H, Jones CK, Zhou J, van Zijl PC, et al. Magnetization transfer contrast-suppressed imaging of amide proton transfer and relayed nuclear overhauser enhancement chemical exchange saturation transfer effects in the human brain at 7 T. Magn Reson Med 2016;75:88–96.
[34] Xu J, Yadav NN, Barshir A, Jones CK, Chan KWY, Zhang J, et al. Variable delay multi-pulse train for fast chemical exchange saturation transfer and relayed-nuclear overhauser enhancement MRI. Magn Reson Med 2014;71:1798–812.
[35] Zhang S, Keupp J, Wang X, Dimitrov I, Madhuranthakam AJ, Lenkinski RE, et al. Z-spectrum appearance and interpretation in the presence of fat: influence of acquisition parameters. Magn Reson Med 2017;79:2731–7.
[36] Heo HY, Zhang Y, Lee DH, Jiang S, Zhao X, Zhou J. Accelerating chemical exchange saturation transfer (CEST) MRI by combining compressed sensing and sensitivity encoding techniques. Magn Reson Med 2016;77:779–86.
[37] Jones CK, Huang A, Xu J, Edden RAE, Schär M, Hua J, et al. Nuclear overhauser enhancement (NOE) imaging in the human brain at 7 T. Neuroimage 2013;77:114–24.
[38] Zaiß M, Schmitt B, Bachert P. Quantitative separation of CEST effect from magnetization transfer and spillover effects by Lorentzian-line-fit analysis of z-spectra. J Magn Reson 2011;211:149–55.
[39] Lu JH, Zhou J, Cai CB, Cai SH, Chen Z. Observation of true and pseudo NOE signals using CEST-MRI and CEST-MRS sequences with and without lipid suppression. Magn Reson Med 2015;73:1615–22.
[40] Zaiss M, Bachert P. Chemical exchange saturation transfer (CEST) and MR Z-spectroscopy in vivo: a review of theoretical approaches and methods. Phys Med Biol 2013;58:221–69.
[41] Chen L, Barker PB, Weiss RG, van Zijl PC, Xu J. Creatine and phosphocreatine mapping of mouse skeletal muscle by a polynomial and Lorentzian line-shape fitting CEST method. Magn Reson Med 2019;81:69–78.
[42] Chen L, Zeng H, Xu X, Yadav NN, Cai SH, Puts NA, et al. Investigation of the contribution of total creatine to the CEST Z-spectrum of brain using a knockout mouse model. NMR Biomed 2017;30:e3834.
[43] Ben-Eliezer N, Shrot Y, Frydman L, Sodickson DK. Parametric analysis of the spatial resolution and signal-to-noise ratio in super-resolved spatiotemporally encoded (SPEN) MRI. Magn Reson Med 2014;72:418–29.
[44] Chen L, Li J, Zhang M, Cai SH, Zhang T, Cai CB, et al. Super-resolved enhancing and edge deghosting (SEED) for spatiotemporally encoded single-shot MRI. Med Image Anal 2015;23:1–14.
[45] Trott O, Iii AGP. $R_{1\rho}$ relaxation outside of the fast-exchange limit. J Magn Reson 2002;154:157–60.
[46] Döpfert J, Zaiss M, Witte C, Schröder L. Ultrafast CEST imaging. J Magn Reson 2014;243:47–53.